Journal of Materials Chemistry B

ROYAL SOCIETY OF CHEMISTRY

PAPER

View Article Online
View Journal | View Issue

Check for updates

Cite this: J. Mater. Chem. B, 2025, 13, 10675

Zeolitic imidazolate frameworks enhanced transfection efficiency of mRNA loaded lipid nanoparticles†

Ruhani Singh,[a] Kerri Bruce,[b] Shen Y Heazlewood,[ad] Jacinta F White,[a] Malisja de Vries,[a] Benjamin W. Muir,[a] Benjamin Cao,[ad] Xavier Mulet,[c] Daniel Layton*[b] and Cara M. Doherty*[a]

Received 19th September 2024,
Accepted 23rd June 2025

DOI: 10.1039/d4tb02101k

rsc.li/materials-b

mRNA vaccines have emerged as a highly effective strategy for the prevention and treatment of various diseases. A critical factor driving the success of mRNA vaccines is the development of advanced multicomponent lipid nanoparticles (LNPs) as a delivery system. As mRNA–LNP technology becomes increasingly integral to vaccine and therapeutic development, there is significant potential to enhance LNP efficiency and build upon the first generation of clinically approved mRNA–LNP products. This can lead to the development of superior formulations that achieve higher protein expression and improved therapeutic outcomes. In this study, we present a novel approach to enhance the transfection efficiency of mRNA–LNPs using ZIF-8 metal–organic framework (MOF). We demonstrate effective encapsulation of mRNA–LNPs within ZIF-8, with preserved structural integrity during dissociation and release. Remarkably, following MOF encapsulation and release, we observed a 3-fold and 8-fold increase in transfection efficiency of the mRNA–LNPs at 48 h in HEK-293 and HCT-116 cells, respectively. Our findings suggest that the presence of ZIF-8 materials with the mRNA–LNPs significantly contributes to their improved transfection and translation efficiency.

Introduction

Over the past two centuries, the emergence of infectious diseases has driven vaccine innovation, culminating recently in the clinical success of mRNA vaccines during the SARS-CoV-2 pandemic. These vaccines demonstrated high safety and efficacy, showcasing the potential of mRNA technology to transform disease prevention and treatment. Their rapid development, precise targeting, and simplified manufacturing have drawn widespread attention and investment.[1,2]

Efficient intracellular delivery of mRNA is fundamental to the success of mRNA vaccines and is predominantly achieved *via* lipid nanoparticles (LNPs), which protect mRNA from degradation and facilitate their cellular uptake.[3,4] Consequently, lipid-based delivery systems—including lipoplexes, liposomes, and LNPs—have gained prominence as versatile and effective carriers for mRNA therapeutics.[4,5] Despite these advances, significant challenges remain: the stringent requirement for cold-chain storage to maintain vaccine stability, the reliance on syringe- and needle-based administration methods, and the need for multiple booster doses to sustain long-term immunity continue to limit broad deployment, particularly in resource-limited settings.[1,4]

Among emerging materials-based strategies, metal–organic frameworks (MOFs)—particularly zeolitic imidazolate framework-8 (ZIF-8)—have shown considerable promise in improving vaccine delivery and stability. One of the earliest studies in this field utilized ZIF-8 to co-encapsulate the model antigen ovalbumin alongside adjuvants, resulting in composite formulations capable of eliciting robust immune responses.[6] Other MOFs based on aluminium, zirconium, and potassium have similarly enabled oral antigen delivery and improved immunogenicity.[7–9] The ZIF-8 MOF remains particularly attractive due to its porosity, pH-responsive degradability, and chemical stability. *In vitro*, it exhibits low to moderate cytotoxicity, influenced by parameters such as particle size, surface chemistry, dose, and exposure time. Particularly, toxicity is cell line-dependent—for example, macrophages and epithelial cells show earlier oxidative stress responses than cancer cells.[10] The toxicity is primarily driven by zinc ion

[a] CSIRO Manufacturing, Private Bag 10, Clayton South, Victoria 3169, Australia. E-mail: cara.doherty@csiro.au
[b] CSIRO Health & Biosecurity, Australian Centre for Disease Preparedness, Geelong, Victoria 3220, Australia. E-mail: daniel.layton@csiro.au
[c] School of Science, RMIT University, Melbourne, Victoria 3000, Australia
[d] Australian Regenerative Medicine Institute, Monash University, Clayton, VIC, Australia

† Electronic supplementary information (ESI) available. See DOI: https://doi.org/10.1039/d4tb02101k

release and reactive oxygen species generation under acidic conditions.[10] Several strategies have been explored to enhance ZIF-8-based therapeutic delivery, notably surface functionalization with molecules like polydopamine, poly-ethylene glycol (PEG), hyaluronic acid, and silica to improve stability and biocompatibility.[11–14] Therefore, the effective assessment of ZIF-8-based platforms depends on both optimized particle design and the use of suitable cell models.

In addition to addressing toxicity concerns, preclinical animal studies have shown that ZIF-8 can also modulate immune responses to subunit vaccines, resulting in enhanced antibody titres.[6,15] A recent study at the Massachusetts Institute of Technology has revealed that ZIF-8 degradation products activate endosomal toll-like receptors, potentiating spike protein immunogenicity.[16] Beyond protein antigens, MOF encapsulation has also been extended to whole-virus platforms. For instance, the Gassensmith group demonstrated that ZIF-8-encapsulated tobacco mosaic virus (TMV) exhibited enhanced thermal and chemical stability.[17–19] Building on this, our group applied ZIF-8 biomimetic mineralization to a commercially available live-viral vaccine—the V4 strain of newcastle disease virus (NDV) and the WSN strain of Influenza A, significantly extending their stability from days to months.[20]

More recently, MOFs have been explored for stabilizing liposomal formulations. Herbert *et al.* immobilized proteoliposomes within ZIFs, conferring exceptional resistance to thermal, mechanical, and chemical stressors.[21] Kumari *et al.* developed a ZIF-8-encapsulated liposomal system suitable for biolistic delivery, offering a viable alternative to needle-based injection.[22] Other studies have demonstrated successful intranasal delivery of ZIF-8-coated liposomes in mice without compromising biocompatibility.[23] These findings suggest that MOF encapsulation could enhance the stability and delivery of more complex lipid nanoparticle systems like the SARS-CoV-2 mRNA vaccines (*e.g.*, BNT162b2, mRNA-1273).

In this study, we present the first demonstration of ZIF-8 biomimetic mineralization applied to mRNA–LNPs. We formulated LNPs containing enhanced green fluorescent protein (eGFP)-encoding mRNA with an ionizable lipid, helper lipid, PEGylated lipid, and cholesterol. These mRNA–LNPs were successfully encapsulated and released from ZIF-8 while maintaining structural integrity and biological function. Remarkably, ZIF-8 encapsulation significantly enhanced mRNA transfection efficiency, offering a promising strategy for the stabilization and delivery of mRNA-based vaccines.

Results and discussion

MOF biomimetic mineralization of LNP@mRNA

To prepare the LNPs used in this study, we vortex-mixed an ethanolic phase composed of the lipids ALC-0315, DSPC, cholesterol, and ALC-0159 with an aqueous phase containing eGFP mRNA, at a 1 : 3 volumetric ratio. The resulting mRNA–LNPs had an N to P ratio of 6, with an average mRNA encapsulation efficiency of 80%, determined by performing a ribogreen assay (Fig. S1, ESI†). This is consistent with previous studies on LNP@mRNA systems, which typically report encapsulation efficiencies ranging between 70–95%.[24,25]

Among the various metal–organic frameworks (MOFs) employed in the biomedical field, zeolitic imidazolate frameworks (ZIFs)—comprising an extended network of Zn^{2+} ions coordinated with 2-methylimidazole linker units—have been extensively explored for applications such as biomolecule encapsulation, drug delivery, and gene therapy. The mechanism of ZIF formation has been well studied and involves the initial association of positively charged zinc ions with the biomolecule, followed by the attachment of the imidazole organic ligands. This process facilitates the formation of pre-nucleation clusters of ZIF-8, leading to controlled biomimetic mineralization on the surface of biomacromolecules.[26]

We have previously applied ZIF-8 for the biomimetic mineralization of live-viral vaccines.[20] The virions in aqueous solution have a negative zeta potential due to their surface proteins, which facilitates interaction with Zn^{2+} ions, resulting in successful encapsulation and thermal stabilization of these vaccines. However, the scenario differs when mRNA is encapsulated within a multi-component lipid nanoparticle (LNP). The inclusion of an ionizable cationic lipid, such as ALC-0315 (theoretical pK_a 6.09), in the LNP formulation used in this study hinders ZIF-8 biomimetic mineralization when the particles are resuspended in nuclease-free water. Cationic surface charge has been shown to hinder ZIF encapsulation.[27] Furthermore, mRNA–LNPs require carefully buffered conditions, as they are osmotically unstable in water.[18] We have previously addressed the challenge of cationic surface charge on proteins using a MOF biomimetic co-encapsulation technique with serum albumin.[28] Other approaches, such as those by Herbert *et al.*, have utilized a solvent solution containing 100 mM NaCl, 1 mM TCEP, and 20 mM MOPS buffered to pH 7.0 to facilitate ZIF biomimetic mineralization of proteo-liposomes.[21] Herein, we used OptiMEM™, a reduced-serum media as the solvent, as it offers both the buffering capacity along with helper constituents to enable ZIF biomimetic co-encapsulation of the LNPs.

A variation in ZIF polymorph can be produced by varying the precursor concentrations.[29] While maintaining a constant precursor ratio of zinc acetate to 2-methylimidazole (1 : 4), we investigated three ZIF-8@LNP@mRNA formulations—A-ZIF-8@LNP@mRNA, B-ZIF-8@LNP@mRNA, and C-ZIF-8@LNP@mRNA, with progressively increasing concentrations of the precursors. Specifically, we prepared the formulations with zinc acetate at 4, 8, and 20 mM, and 2-methylimidazole at 16, 32, and 80 mM, respectively. The optimization of precursor concentrations aimed to maximize ZIF-8 encapsulation of LNPs while minimizing the potential toxicity associated with excess ZIF material, knowing that toxicity is dose-dependent. All ZIF-8@LNP@mRNA syntheses and subsequent post-processing were conducted in proprietary OptiMEM™ media.

The aqueous synthesis of ZIF-8 at a low molar ratio of precursors (1 : 4) typically favors the formation of an amorphous material (aZIF).[30,31] Consistent with expectations, our synthesis conditions resulted in an amorphous coordination polymer.

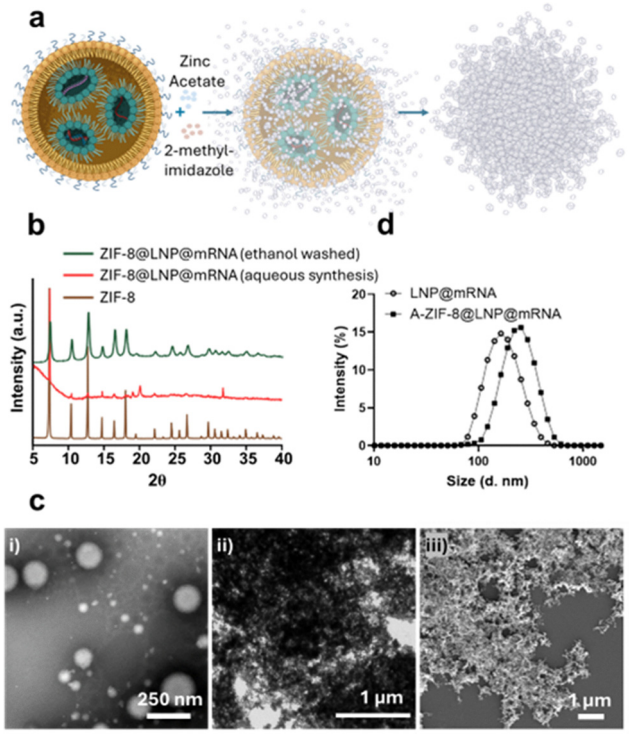

Fig. 1 Synthesis and characterization of ZIF-8@LNP@mRNA prepared *via* the biomimetic mineralization technique. (a) Schematic illustration of the proposed mechanism: the presence of LNPs in a buffered medium increases the local concentration of precursors, facilitating the formation of ZIF-8 prenucleation clusters, leading to the biomimetic growth of ZIF-8 around the LNPs. (b) Powder X-ray diffraction (PXRD) spectra demonstrate the similarity between ZIF-8@LNP@mRNA (ethanol washed; crystalline) and the control ZIF-8 MOF, whereas the aqueous synthesis resulted in ZIF-8@LNP@mRNA (aqueous synthesis; amorphous) with an amorphous phase. (c) Transmission electron microscopy (TEM) images show LNP@mRNA (i) (scale – 250 nm) and ZIF-8@LNP@mRNA (ii) (scale – 1 µm), while the scanning electron microscopy (SEM) image of ZIF-8@LNP@mRNA (iii) (scale – 1 µm) highlights the structural characteristics. (d) The average hydrodynamic diameter of the LNP@mRNA increased from 174 nm to 260 nm after encapsulation and release from the ZIF-8@LNP@mRNA, as observed using dynamic light scattering (DLS).

However, to confirm the composition of ZIF-8, it was necessary to obtain a crystalline phase. To achieve this, the amorphous A-ZIF-8@LNP@mRNA composite was washed with ethanol, which resulted in the formation of a crystalline ZIF-8 phase, as confirmed by X-ray diffraction (XRD) analysis shown in Fig. 1b. Fig. 1c(ii and iii) presents TEM and SEM images of the A-ZIF 8@LNP@mRNA precipitate, revealing a dense deposit of the amorphous flocculate. When ethanol post-processing was applied, the composite transitioned to crystalline ZIF 8@LNP@mRNA (ethanol washed) crystals, exhibiting a truncated rhombic dodecahedral morphology, rather than the typical rhombic dodecahedron morphology of control ZIF-8 (Fig. S2, ESI†).

The functional integrity of the ZIF-8 encapsulated LNPs was evaluated *in vitro* after releasing the mRNA–LNPs from their ZIF scaffolds using a sodium citrate buffer (pH 5.0, 50 mM). ZIF-8 is known to be unstable and dissociates rapidly in acidic sodium citrate buffer. Moreover, citrate ions chelate Zn^{2+}, further breaking the coordination bonds within the ZIF-8 MOF, facilitating the release of encapsulated mRNA–LNPs. We confirmed using TEM analysis, that the LNPs released from the MOF maintained their structural integrity. Additionally, we observed an increase in their hydrodynamic size from an average of 174 nm (PdI: 0.3) to an average of 260 nm (PdI: 0.2) using dynamic light scattering (DLS), as shown in Fig. 1d.

Fig. 2a shows energy-dispersive X-ray spectroscopy (EDS) analysis of A-ZIF-8@LNP@mRNA. The EDS confirms the presence of expected elements in the mRNA-encapsulating LNP, including C, O, N, P, and Zn. Zinc from the ZIF-8 is distributed throughout the sample but is especially concentrated around the spherical moieties in the flocculate, confirming the ZIF mineralized composition of the LNP formulations. The elemental composition (weight %) for each sample is detailed in the corresponding table in Fig. S3 (ESI†). After sodium citrate dissolution of the ZIF, EDS of the sample showed a limited presence of zinc inside the emerging carbon-rich spherical nanoparticles, while much of the

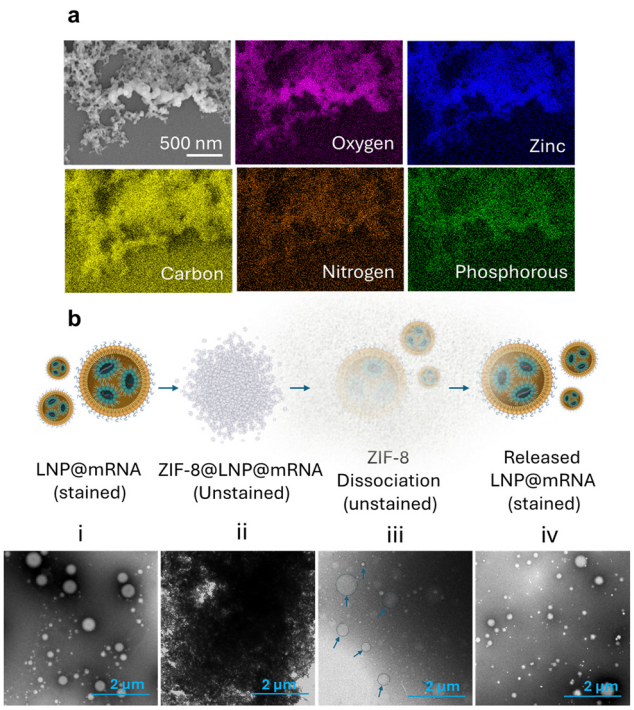

Fig. 2 Elemental analysis of ZIF-8@LNP@mRNA and transmission electron microscopy (TEM) visualization of ZIF-8 encapsulation and release of LNP@mRNA. (a) Energy-dispersive X-ray spectroscopy (EDS) analysis of A-ZIF-8@LNP@mRNA confirms the presence of expected elements in the mRNA-encapsulating LNP, including O, C, and N, along with Zn from ZIF-8 (blue) and P from the LNP@mRNA (green). These elements are distributed throughout the sample, with Zn particularly concentrated around the spherical moieties in the flocculate, confirming the ZIF mineralized composition of the LNP formulations (scale – 500 nm). The sequence of events is depicted in schematic (b), with corresponding steps (i) to (iv) captured using TEM images: (i) LNP@mRNA are encapsulated within the ZIF-8 MOF, forming an amorphous composite (ZIF-8@LNP@mRNA); (ii) sodium citrate buffer (pH 5.0, 50 mM) is then used to disintegrate the ZIF-8, with pointers highlighting individual nanoparticles released upon MOF disintegration. (iii), resulting in the release of structurally intact LNP@mRNAs (iv).

dissolved zinc and sodium salts were observed around these nanostructures (Fig. S4, ESI†).

TEM, with its exceptional nanoscale resolution, was used to visualize the sequence of events from LNP biomimetic mineralization in the ZIF MOF to the subsequent release using citrate buffer prior to transfection assays. Fig. 2b(i) shows the unilamellar LNPs revealed by negative contrast using a phosphotungstic acid negative-stain. The LNPs exhibited a wide size distribution, ranging from 50 nm to 500 nm, which reflects the variability introduced by manual vortex-mixing during preparation. The formation of ZIF-8@LNP@mRNA produced a floc, as shown in the electron image in Fig. 2b(ii). Upon the addition of sodium citrate release buffer, the ZIF disintegrates, as captured in the unstained image in Fig. 2b(iii), where LNPs are seen emerging from the partially dissolved, electron-dense ZIF material. After complete dissolution, the negatively stained LNPs in Fig. 2b(iv) confirms that the structural integrity of the released LNPs remains intact following the encapsulation and release process.

Efficiency of the ZIF-8@LNP@mRNA formulations

The transfection efficiency and mRNA translation of the three formulations—A-ZIF-8@LNP@mRNA, B-ZIF-8@LNP@mRNA, and C-ZIF-8@LNP@mRNA—were compared to LNP@mRNA in HEK-293 and HCT-116 cells. The experimental process is illustrated in Fig. 3a. On the day of transfection, the culture media was removed from sub-confluent adherent cells plated in a 96-well plate and replaced with each of the formulation types (LNP@mRNA, A-ZIF-8@LNP@mRNA, B-ZIF-8@LNP@mRNA, and C ZIF 8@LNP@mRNA) diluted in reduced serum media (OptiMEM™) at a 2.5 μg mL^{-1} mRNA loading. The cells were incubated with these different formulations for 24 hours, after which the media was replaced with normal culture media containing 10% FBS. Cells were continuously imaged, every 3 hours for a total period of 48 hours. In parallel, a lactate dehydrogenase (LDH) assay was performed at the 24-hour time point to assess cytotoxicity, determined by the level of plasma membrane damage (Fig. S5, ESI†).

Transfection efficiency (%) was quantified by measuring the green-fluorescent area as a fraction of the total phase area confluence, while protein expression (translation efficiency) was assessed by the total green integrated intensity. Fig. 3b and d show the transfection efficiency of LNP@mRNA, A-ZIF-8@LNP@mRNA, B-ZIF-8@LNP@mRNA, and C-ZIF-8@LNP@mRNA in HEK-293 and HCT-116 cells, respectively. LNP@mRNA showed a delayed GFP expression, which began 12 hours post-incubation and increased sharply to a mean transfection efficiency of 45% at 24 hours. As shown in Fig. 3c, the integrated green intensity, representing the amount of protein produced, also increased between 18 and 24 hours, reaching a peak of 6.6×10^6 units at 24 hours. Upon the addition of serum-containing media at 24 hours (indicated by a dotted line), the number of cells treated with LNP@mRNA doubled over the next 24 hours (Fig. S6, ESI†). However, the increase in GFP-expressing cells was not proportional to the increase in confluence, leading to a drop in transfection efficiency to an average of 25% at 48 hours. The GFP protein

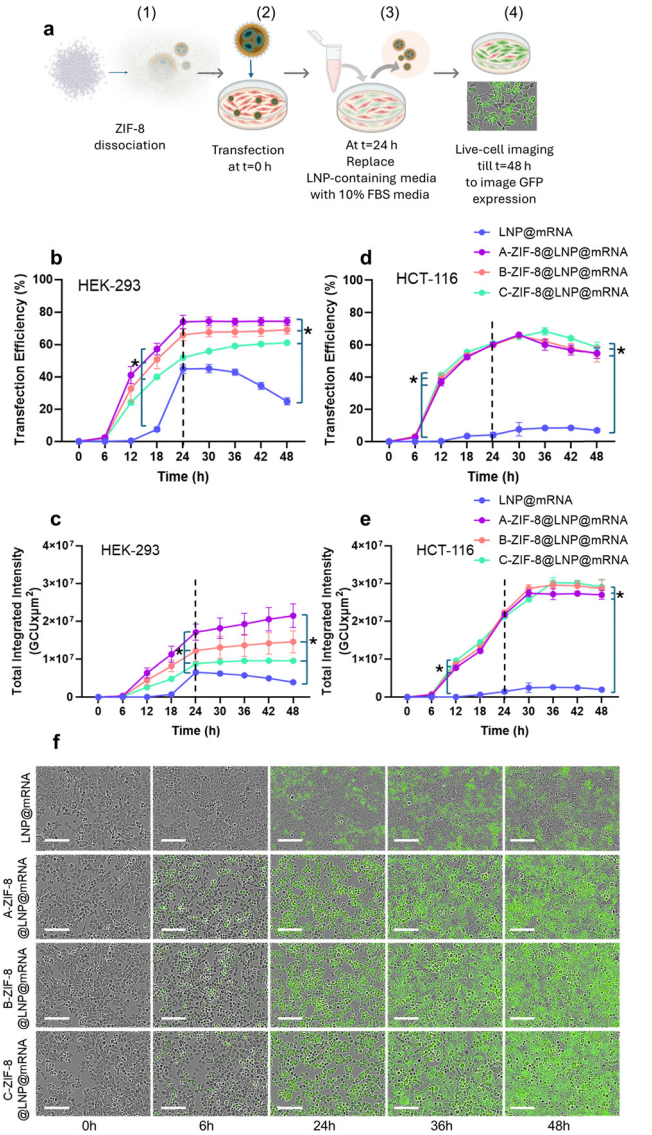

Fig. 3 Transfection efficiency of LNP@mRNA and ZIF-8@LNP@mRNA formulations evaluated in HEK-293 and HCT-116 cells. (a) Schematic representation of the experimental methodology for transfection experiments. (1) ZIF-8@LNP@mRNA formulations were dissociated to release LNPs using a sodium citrate buffer (50 mM, pH 5.0) and then (2) added to adherent cells cultured in OptiMEM media. After a 24-hour incubation period, (3) the media containing the formulations was replaced with cell culture media supplemented with 10% serum. The cells were monitored continuously during the initial 24 hours and (4) for an additional 24 hours to assess phase area confluence, green fluorescent protein expression area, and intensity in the cells. The control and test formulations included: (1) OptiMEM media, (2) LNP@mRNA, (3) A-ZIF-8@LNP@mRNA, (4) B-ZIF-8@LNP@mRNA, and (5) C-ZIF-8@LNP@mRNA. Transfection efficiencies in HEK-293 cells (b) and HCT-116 cells (d), defined by the green area fraction of the total phase area in each well (n = 3), were plotted as shown. Corresponding total integrated intensity values are presented in (c) and (e), respectively. The dotted line at 24 hours indicates the time point at which the media conditions were changed. Chronological representative images from HCT-116 cells treated with each test LNP formulation are shown in (f) scale – 150 μm. Data were analysed by ordinary two-way ANOVA, comparing mean values of the different formulations at a single time point (*; $p < 0.05$).

levels also decreased, as evidenced by a reduction in the integrated green intensity to 4×10^6 units at 48 hours.

In contrast, A-ZIF-8@LNP@mRNA, B-ZIF-8@LNP@mRNA, and C-ZIF-8@LNP@mRNA exhibited more rapid GFP expression profiles in HEK-293 cells, with significantly higher mean transfection efficiencies of 57%, 51%, and 40% at 18 hours, and 74%, 66%, and 52% at 24 hours, respectively. Beyond 24 hours, the fraction of transfected cells plateaued for A-ZIF-8@LNP@mRNA and B-ZIF-8@LNP@mRNA, indicating that, unlike the stalled GFP expression in LNP@mRNA-treated cells, the number of green-fluorescent cells increased in proportion to the phase area confluence for these ZIF-8 formulations. The green integrated intensity continued to increase, indicating consistently higher protein production for all three ZIF-8 formulations. Notably, A-ZIF-8@LNP@mRNA demonstrated a significantly higher amount of GFP, with a 5-fold increase compared to LNP@mRNA at 48 hours.

Overall, there was no significant difference in transfection efficiency between A-ZIF-8@LNP@mRNA and B-ZIF-8@LNP@mRNA. However, A-ZIF-8@LNP@mRNA consistently outperformed C-ZIF-8@LNP@mRNA from 18 hours onwards. A-ZIF-8@LNP@mRNA was the most optimal formulation, showing 7.6-, 1.6-, and 3-fold higher transfection efficiency than LNP@mRNA at 18, 24, and 48 hours, respectively.

Due to their epithelial origin, HCT-116 cells are considered difficult to transfect, which is evident in our results (Fig. 3d), where the control LNP@mRNA achieved a maximum transfection efficiency of only 8.5% in HCT-116 cells, compared to 45% in HEK-293 cells. Recent efforts to address this limitation have focused on developing novel lipid formulations. For example, Qian *et al.* reported a newly synthesized lipid, S-1, which demonstrated significantly enhanced expression in HCT-116 cells, surpassing that in HEK-293 cells over a 24-hour period. Notably, our ZIF-8@LNP@mRNA formulation achieved comparable transfection efficiencies in both HCT-116 and HEK-293 cells, suggesting improved performance in hard-to-transfect cell lines.[32] While LNP-treated HCT-116 cells showed a mean transfection efficiency of 3.5% at 18 hours, over 50% of cells were successfully transfected using the ZIF-8 formulations at the same time point. All three ZIF-8@LNP@mRNA formulations significantly outperformed LNP@mRNA from 12 hours onwards, with no significant differences among A-ZIF-8@LNP@mRNA, B-ZIF-8@LNP@mRNA, and C ZIF 8@LNP@mRNA at any time point. The maximum mean transfection efficiency reached 66% for A-ZIF-8@LNP@mRNA and B-ZIF-8@LNP@mRNA at 30 hours, and 69% for C-ZIF-8@LNP@mRNA at 36 hours. GFP protein production steadily increased to 2.7×10^7, 2.9×10^7, and 2.6×10^7 units for A-ZIF-8@LNP@mRNA, B-ZIF-8@LNP@mRNA, and C-ZIF-8@LNP@mRNA, respectively—at least 10 times higher than the 2.5×10^6 units for LNP@mRNA at 30 hours. Between 30 and 48 hours, despite the recovery in cell density (Fig. S6, ESI†) and a plateaued intensity indicating further GFP expression, the transfection efficiency values dropped to 55%, 54%, and 58%, respectively, for A-ZIF-8@LNP@mRNA, B-ZIF-8@LNP@mRNA, and C-ZIF-8@LNP@mRNA, remaining significantly higher than the 7% mean for LNP@mRNA. Fig. 3f shows representative images from each of the LNP@mRNA and ZIF-8@LNP@mRNA treated wells. (See corresponding images for HEK-293 cells in Fig. S8, ESI†). A separate experiment with A549 cells using a shorter 5-hour incubation (compared to the 24-hour incubation used for HEK-293 and HCT-116 cells) showed a similar enhancement in transfection efficiency, consistent with observations in HEK-293 and HCT-116 cells (Fig. S7, ESI†). However, the use of a different cell type and incubation condition led to an earlier plateau in GFP expression at the 12-hour time point.

ZIF-8 attributed enhanced transfection is independent of ZIF-8 encapsulation

The initial aim of our study was to apply biomimetic mineralization of mRNA–LNPs for developing needle-free and thermostable vaccine formulations. However, we discovered that the ZIF-8@LNP@mRNA formulations we developed significantly enhanced the transfection and translation efficiency of LNPs. To determine whether this enhancement is due to the ZIF-8 encapsulation or structural changes in the mRNA–LNPs upon release, we compared B-ZIF-8@LNP@mRNA with B-ZIF 8 + LNP@mRNA, where B-ZIF-8 was separately synthesized and added to LNP@mRNA. Both formulations were dissociated using sodium citrate buffer (50 mM, pH 5.0) before transfection experiments. Fig. 4a and b display the transfection efficiency in HEK-293 and HCT-116 cells. No significant difference in transfection efficiency was observed between the two formulations in both cell lines, suggesting that the enhancement in transfection efficiency is independent of ZIF-8 encapsulation. We propose that the presence of ZIF-8 dissociates is responsible for the increased mRNA transfection and translation efficiency. Nonetheless, ZIF-8 encapsulation could offer additional benefits, such as enhanced thermostability and alternative administration routes, as indicated by other studies.[21,22,33,34]

Reviewing prior art in the field of ZIF-8-vaccine development, most studies have employed nanoZIF-8 as an intracellular delivery vehicle for intracellular delivery of non-replicating viral vaccines and sub-unit vaccines.[6,15–17,19,33,35–37] Conversely, ZIF-8 can also serve as a protective coating, to be released or dissociated just before vaccine administration.[20] This application depends on the cargo; while nucleic acids and proteins require a nanocarrier for intracellular delivery, live-viral and

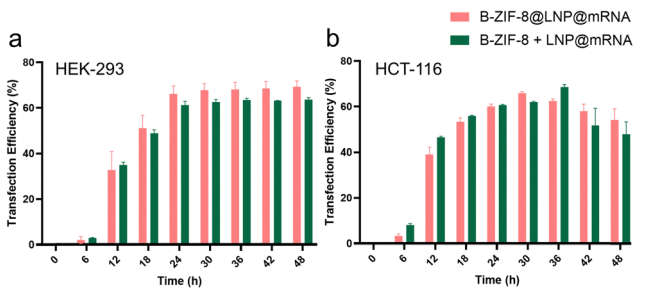

Fig. 4 A comparison of the transfection efficiencies of B-ZIF-8 + LNP@mRNA and B-ZIF-8@LNP@mRNA, formulations containing the ZIF-8 added to LNP@mRNA and ZIF-8 encapsulated LNP@mRNA, respectively in (a) HEK-293 and (b) HCT-116 cells.

non-viral agents like LNPs are self-sufficient for cell invasion and endocytosis.

The ZIF-8 MOF structure comprises a lattice of tetrahedral units made of zinc ions coordinated with four imidazole molecules. The coordination bond can easily dissociate with changes in pH or the presence of a chelator. This dissociation can occur exogenously using sodium citrate buffer (50 mM, pH 5.0) or intracellularly after endocytosis in lysosomal and endosomal compartments, releasing the cargo vaccine along with ZIF-8 disintegration products containing imidazolate and Zn^{2+}.

Both imidazole and zinc have been associated with enhancing vaccine response, and we postulate that they may have a synergistic effect in the context of ZIF-8. Imidazole is present in many commercial toll-like receptor (TLR) agonists,[38,39] which are critical to the innate immune system. TLRs 3, 7, 8, and 9, located on endosomal membranes, trigger immune responses upon encountering viral or bacterial RNA. Interestingly, recent reports suggest that ZIF-8 induces TLR-3, 7, and 9 expressions, initiating proinflammatory responses and thereby enhancing immunogenicity.[9] This enhancement is mainly attributed to the 2-methylimidazole degradation products, with Zn^{2+} shown not to activate TLR-7, TLR-8, or TLR-9 in reporter cells. The study also compared ZIF-8 with mRNA–LNPs, suggesting that LNP@mRNA immune activation is driven by monocyte-derived dendritic cells and the cDC1 subset of conventional DCs, while TLR-7 activation by ZIF-8 is unique among other nanodelivery vehicles.

Zinc homeostasis is crucial for normal immune function.[40] The metalloimmunological effects of zinc have been extensively studied, showing that Zn^{2+} enhances the transfection efficiency of various polymeric and lipoplex-based transfection agents. These studies link Zn^{2+} to (1) increased endocytosis through cell membrane-metal coordination, (2) enhanced endosomal escape *via* strong interactions between zinc and phosphatidylserine in the endosomal membrane and increased 'proton-sponge' effect leading to endosome swelling and rupture, and (3) excellent anti-serum or low-protein binding capability.[41–45] These properties make Zn^{2+} advantageous for mRNA therapeutics, where only 2–8% of mRNA typically escapes the endosome to be released into the cytosol.[46] Additionally, zinc's coordination with nucleic acid phosphate groups aids in maintaining the integrity of the nucleic acids, leading to higher antigen production and improved immune response.[47,48]

Conclusion

Despite significant advancements in mRNA–LNP vaccines, challenges remain in maximizing LNP efficiency, which is critical for realizing the therapeutic potential of mRNA-based therapies. Transfection efficiency—defined as the percentage of cells successfully expressing the target protein after LNP delivery—depends on factors such as LNP formulation, cellular uptake, endosomal escape, and mRNA translation efficiency.[49] Optimizing these steps offers opportunities to enhance transfection efficiency and therapeutic outcomes.

Inspired by recent studies on ZIF encapsulation of liposomes and proteoliposomes, we explored the biomimetic mineralization of mRNA-loaded multi-lipid nanoparticles. During this investigation, we discovered that ZIF-8 significantly enhances LNP transfection efficiency. This effect is not linked to structural or compositional changes in the LNPs upon encapsulation but is attributed to the presence of ZIF-8 dissociates, which enhance transfection efficiency. Based on literature, Zn^{2+} aids in mRNA cytosolic delivery, boosting transfection efficiency and potentially increasing antibody production *in vivo*, while imidazolates can trigger an innate immune response. We hypothesize that the imidazole and zinc components of ZIF-8 may work synergistically to enhance both transfection efficiency and immunogenicity.

The results of this preliminary study suggest that ZIF-8 is a safe, facile, and cost-effective additive that could improve vaccine efficiency. Additionally, when encapsulated within ZIF 8, formulations may be suitable for needle-free administration and ambient storage. Given that ZIF-8 dissociation is pH-dependent, encapsulated formulations could be adapted for single-dose, slow-release vaccines, which have been shown to elicit stronger immune responses. Overall, these findings warrant further investigation into the role and mechanism of ZIF-8 and its dissociates in improving the efficacy of mRNA–LNP vaccines, potentially utilizing these novel materials as additives to mRNA–LNP formulations.

Experimental

Materials

All materials, zinc acetate dihydrate (≥99%), 2-methylimidazole (99%), Tris Buffered Saline (TBS) tablets, sodium citrate dihydrate, citric acid, ethanol, DNAse/RNAse free water, OptiMEM media were purchased commercially. All buffers were sterilized by autoclaving at 121 °C, 15 psi for 1 h.

Cell culture: HEK-293 cells were maintained at 37 °C, 5% CO_2 in complete cell culture medium containing DMEM (Glutamax), 10% foetal bovine serum (FBS), 2 mM L-glutamine (GlutaMAX), 1% NEAA. The HCT-116 cells were maintained in McCoys 5a modified media, 10% heat inactivated FBS, 2 mM L-glutamine (GlutaMAX). The A549 cells were maintained in F12 media, 10% heat inactivated FBS and glutamax. All the cells were subcultured every 3–4 d. One day prior to the transfection, cells were seeded at a density of 2.0×10^4 cells per well in 96 well plates in complete cell culture media.

Preparation of lipid nanoparticles (LNPs)

There are multiple comparable methods such as pipette mixing, vortex mixing, and microfluidic mixing that can be used to efficiently mix and manufacture multi-lipid nanoparticles.[50] Solution (a), A 90 μL aqueous solution of eGFP mRNA was prepared by diluting 15 μL of stock mRNA (ApexBio ARCA modified EGFP mRNA; #R1001, 996 nucleotides; supplied as 1 mg mL^{-1} in 1 mM sodium citrate, pH 6.4) in 75 μL of sodium citrate buffer (pH 4.0, 10 mM).

Solution (b), A 30 μL ethanolic solution containing, an ionizable lipid ALC-0315 (6-((2-hexyldecanoyl)oxy)-*N*-(6-((2-hexyldecanoyl)oxy)hexyl)-*N*-(4-hydroxybutyl)hexane-1-aminium), a helper lipid DSPC (Distearoylphosphatidylcholine), Cholesterol, and a PEGylated lipid ALC-0159 (Methoxypolyethyleneglycoloxy(2000)-*N*,*N*-ditetradecylacetamide) in a molar ratio of 46.3 : 9.4 : 42.7 : 1.6 was prepared. The lipids and the molar ratios used herein are similar to those used for BNT162b2; Comirnaty *i.e.* the SARS-CoV-2 mRNA vaccine manufactured by the Pfizer-BioNTech collaboration.[51] For multiple experiments within a period of 2 months, we prepared this solution in bulk and stored at 20 °C until further use. To prepare LNPs, Solution (b) is added to Solution (a) in a 1.5 mL tube with constant vortex mixing for 30 sec. The LNP solution formed herein is immediately dialyzed using a Pur-A-Lyzer™ dialysis kit (Sigma Aldrich, #PURN60030, capacity 10 250 μL, MWCO 6–8 kDa) against Tris Buffered Saline (50 mM, pH 7.6) for a period of 1 h. Dialysed LNP solution is collected and made to 150 μL using Tris Buffered Saline (50 mM, pH 7.6). The 150 μL LNP solution is further diluted 4 times in reduced serum media (OptiMEM media; ThermoFisher Scientific #31985062; containing sodium bicarbonate buffer system (2.4 g L^{-1}), insulin, transferrin, hypoxanthine, thymidine, and trace elements to allow for a reduction in serum supplementation) to make 600 μL of LNPs in OptiMEM media, Solution (c) for further use.

Preparation of ZIF@LNP formulations

Stock solutions of the ZIF precursors, the organic ligand 2-methylimidazole and the metal salt, zinc acetate was prepared in OptiMEM media at 320 mM and 80 mM, respectively. To a 300 μL aliquot of LNP solution (c) each, 150 μL of 32 mM, 64 mM and 160 mM of 2 methylimidazole were added and carefully mixed by pipetting for preparation of ZIF(A), ZIF(B), and ZIF(C) formulations, respectively. This was followed by an addition of 150 μL zinc acetate solution at a concentration of 8 mM, 16 mM, and 40 mM and soft pipette mixing for preparation of ZIF(A), ZIF(B), and ZIF(C) formulations, respectively. Flocs appeared immediately for ZIF(C) and slowly for ZIF(B) and ZIF(A). The solutions were left to sit over a period of 15 min at room temperature. The pellet was washed and collected by centrifugation at 14 000 × *g* for 5 min to give ZIF(A), ZIF(B), and ZIF(C) formulations, respectively. Prior to cell experiments, the LNPs from the ZIF formulations were recovered by exfoliating the ZIF using a sodium citrate buffer (50 mM, pH 5.0). To the above prepared pellets, 300 μL of the sodium buffer was added and gently mixed by pipetting, until the flocculation turned clear.

In vitro transfection experiments

Solution (c) as prepared in Section 4.1; LNPs in OptiMEM media and the LNPs recovered from ZIF formulations, as prepared in Section 4.2 were all diluted 10 times in OptiMEM media to a final mRNA concentration of 2.5 μg mL^{-1} or 2500 ng mL^{-1} before adding to cells. Cell culture media was completely removed and 100 μL of all samples were added to each well (96 well plate). Cell culture plates were continuously imaged every 3 h using the Incucyte® Live Cell Analysis system to observe the phase area cell confluence and the green fluorescence signal from eGFP expression. For HEK-293 and HCT-116 cells, after a period of 24 h, the samples were removed and replaced with complete cell culture media containing 10% FBS. The plate was imaged every 3 hours on the Incucyte® for a period of 48 h. Experiments were performed in triplicate ($n = 3$) and repeated twice. For the A549 cells, the samples were removed and replaced with complete cell culture media containing 10% FBS after 5 h. A549 cells were also continuously observed on the Incucyte® for a period of 48 h.

Characterisation techniques

Dynamic light scattering (DLS). Dynamic-light scattering was measured with a Malvern Zeta- sizer Nano ZS. A disposable cuvette was used at 25 °C with a 633 nm laser source, a medium refractive index of 1.33, a material refractive index of 1.51, and a scattering angle of 175°.

Transmission electron microscopy (TEM). Carbon-coated grids (EMSCF200H–CU-TH, ProSciTech) were glow discharged to render them hydrophilic. A 10 μL drop of sample was applied to an upturned grid held in anti-capillary forceps, over moist filter paper, and left for 10 min to adsorb. The excess sample was then removed with filter paper. If stained, the grid was then inverted onto a drop of 2% PTA stain, pH 6.9 on Parafilm, for 1 min. The grid was removed, the stain wicked away with filter paper and allowed to dry before viewing in the microscope. The samples were examined using a Tecnai 12 transmission electron microscope (FEI, Eindhoven, The Netherlands) at an operating voltage of 120 kV. Images were recorded using a FEI Eagle 4k × 4k CCD camera and AnalySIS v3.2 camera control software (Olympus).

Scanning electron microscopy (SEM) and energy dispersive spectroscopy (EDS). Samples were mounted either on carbon tape or silicon wafer and then put on aluminium stubs. The samples were coated with conductive Gold using Cressington HR 208HR sputter coater for 20 s to give a 3 nm coating. Samples were imaged using a Zeiss Merlin FESEM at an accelerating voltage of 3 kV in the secondary electron or in lens mode depending on magnification. Magnification is indicated with the scale bars in each image. Elemental composition (EDS) was conducted using Oxford Instruments Extreme 100 mm^2 windowless SSD detector at an accelerating voltage of 5 kV.

Statistical analysis. All values reported are means ± SD. Data were analysed by ordinary two-way ANOVA comparing mean values of the different parameters at a single time point ($p < 0.05$). Either Tukey's multiple comparison, or the Holm–Sidak multiple comparisons (*, $p < 0.05$) were performed with a single pooled variance and family-wise alpha threshold/confidence level of 0.05 (95% CI). Tables for all statistical comparisons and the corresponding adjusted *P* values are available in the ESI.†

Conflicts of interest

There are no conflicts to declare.

Data availability

The data supporting this article have been included as part of the ESI.†

Acknowledgements

RS and CMD acknowledge CSIRO Strategic funding for this work. CMD acknowledges the Veski Inspiring Women fellowship for support. Brenda Williams, Manufacturing, CSIRO is acknowledged for her assistance in cell culturing and maintenance.

References

1 N. Pardi, M. J. Hogan, F. W. Porter and D. Weissman, *Nat. Rev. Drug Discovery*, 2018, **17**, 261–279, DOI: **10.1038/nrd.2017.243**.

2 U. Sahin, A. Muik, E. Derhovanessian, I. Vogler, L. M. Kranz, M. Vormehr, A. Baum, K. Pascal, J. Quandt, D. Maurus, S. Brachtendorf, V. Lörks, J. Sikorski, R. Hilker, D. Becker, A. K. Eller, J. Grützner, C. Boesler, C. Rosenbaum, M. C. Kühnle, U. Luxemburger, A. Kemmer-Brück, D. Langer, M. Bexon, S. Bolte, K. Karikó, T. Palanche, B. Fischer, A. Schultz, P.-Y. Shi, C. Fontes-Garfias, J. L. Perez, K. A. Swanson, J. Loschko, I. L. Scully, M. Cutler, W. Kalina, C. A. Kyratsous, D. Cooper, P. R. Dormitzer, K. U. Jansen and Ö. Türeci, *Nature*, 2020, **586**, 594–599, DOI: **10.1038/s41586-020-2814-7**.

3 U. Sahin, K. Karikó and Ö. Türeci, *Nat. Rev. Drug Discovery*, 2014, **13**, 759–780, DOI: **10.1038/nrd4278**.

4 X. Hou, T. Zaks, R. Langer and Y. Dong, *Nat. Rev. Mater.*, 2021, **6**, 1078–1094, DOI: **10.1038/s41578-021-00358-0**.

5 R. Verbeke, I. Lentacker, S. C. De Smedt and H. Dewitte, *J. Control Release*, 2021, **333**, 511–520, DOI: **10.1016/j.jconrel.2021.03.043**.

6 Y. Zhang, F. Wang, E. Ju, Z. Liu, Z. Chen, J. Ren and X. Qu, *Adv. Funct. Mater.*, 2016, **26**, 6454–6461, DOI: **10.1002/adfm.201600650**.

7 Y. B. Miao, W. Y. Pan, K. H. Chen, H. J. Wei, F. L. Mi, M. Y. Lu, Y. Chang and H. W. Sung, *Adv. Funct. Mater.*, 2019, **29**, 1904828, DOI: **10.1002/adfm.201904828**.

8 Y. Qi, L. Wang, H. Guo, Y. Pan, Z. Xie, N. Jin and Y. Huang, *Biomater. Sci.*, 2019, **7**, 4022–4026, DOI: **10.1039/c9bm01145e**.

9 C. Li, C. Chen, Y. Wei, M. Tan, S. Zhai, J. Zhao, L. Wang and T. Dai, *Drug Delivery*, 2021, **28**, 2594–2602, DOI: **10.1080/10717544.2021.2012306**.

10 M. Hoop, C. F. Walde, R. Riccò, F. Mushtaq, A. Terzopoulou, X.-Z. Chen, A. J. DeMello, C. J. Doonan, P. Falcaro, B. J. Nelson and J. Puigmarti-Luis, *Appl. Mater. Today*, 2018, **11**, 13–21, DOI: **10.1016/j.apmt.2017.12.014**.

11 L. Peng, J. Qiu, L. Liu, X. Li, X. Liu and Y. Zhang, *Drug Delivery*, 2022, **29**, 1075–1085, DOI: **10.1080/10717544.2022.2058649**.

12 Q. Wang, M. Li, X. Sun, N. Chen, S. Yao, X. Feng and Y. Chen, *J. Mater. Chem. B*, 2023, **11**, 1782–1797, DOI: **10.1039/D2TB02361J**.

13 S. Yu, S. Wang, Z. Xie, S. Yu, L. Li, H. Xiao and Y. Song, *Colloids Surf., B*, 2021, **203**, 111759, DOI: **10.1016/j.colsurfb.2021.111759**.

14 S. Z. Ren, D. Zhu, X. H. Zhu, B. Wang, Y. S. Yang, W. X. Sun, X. M. Wang, P. C. Lv, Z. C. Wang and H. L. Zhu, *ACS Appl. Mater. Interfaces*, 2019, **11**, 20678–20688, DOI: **10.1021/acsami.9b04236**.

15 G. Zhang, X. Fu, H. Sun, P. Zhang, S. Zhai, J. Hao, J. Cui and M. Hu, *ACS Appl. Mater. Interfaces*, 2021, **13**, 13978–13989, DOI: **10.1021/acsami.1c00706**.

16 S. K. Alsaiari, S. Nadeef, J. L. Daristotle, W. Rothwell, B. Du, J. Garcia, L. Zhang, M. Sarmadi, T. A. Förster, N. Menon and Lin S. Q. Lin, *Sci. Adv.*, 2024, **10**, eadj6380, DOI: **10.1126/sciadv.adj6380**.

17 S. Li, M. Dharmarwardana, R. P. Welch, C. E. Benjamin, A. M. Shamir, S. O. Nielsen and J. J. Gassensmith, *ACS Appl. Mater. Interfaces*, 2018, **10**, 18161–18169, DOI: **10.1021/acsami.8b01369**.

18 S. Li, M. Dharmarwardana, R. P. Welch, Y. Ren, C. M. Thompson, R. A. Smaldone and J. J. Gassensmith, *Angew. Chem.*, 2016, **128**, 10849–10854, DOI: **10.1002/ange.201604879**.

19 M. A. Luzuriaga, R. P. Welch, M. Dharmarwardana, C. E. Benjamin, S. Li, A. Shahrivarkevishahi, S. Popal, L. H. Tuong, C. T. Creswell and J. J. Gassensmith, *ACS Appl. Mater. Interfaces*, 2019, **11**, 9740–9746, DOI: **10.1021/acsami.8b20504**.

20 R. Singh, J. F. White, M. de Vries, G. Beddome, M. Dai, A. G. Bean, X. Mulet, D. Layton and C. M. Doherty, *Acta Biomater.*, 2022, **142**, 320–331, DOI: **10.1016/j.actbio.2022.02.002**.

21 F. C. Herbert, S. S. Abeyrathna, N. S. Abeyrathna, Y. H. Wijesundara, O. R. Brohlin, F. Carraro, H. Amenitsch, P. Falcaro, M. A. Luzuriaga, A. Durand-Silva and S. D. Diwakara, *Nat. Commun.*, 2021, **12**, 2202, DOI: **10.1038/s41467-021-22285-y**.

22 S. Kumari, Y. H. Wijesundara, T. S. Howlett, M. Waliullah, F. C. Herbert, A. Raja, I. Trashi, R. A. Bernal and J. J. Gassensmith, *Proc. Natl. Acad. Sci. U. S. A.*, 2023, **120**, e2218247120, DOI: **10.1073/pnas.2218247120**.

23 S. Kumari, T. S. Howlett, R. N. Ehrman, S. Koirala, O. Trashi, I. Trashi, Y. H. Wijesundara and J. J. Gassensmith, *Chem. Sci.*, 2023, **14**, 5774–5782, DOI: **10.1039/d3sc00500c**.

24 K. J. Hassett, K. E. Benenato, E. Jacquinet, A. Lee, A. Woods, O. Yuzhakov, S. Himansu, J. Deterling, B. M. Geilich, T. Ketova and C. Mihai, *Mol. Ther. Nucleic Acids*, 2019, **15**, 1–11, DOI: **10.1016/j.omtn.2019.01.013**.

25 M. D. Buschmann, M. J. Carrasco, S. Alishetty, M. Paige, M. G. Alameh and D. Weissman, *Vaccines*, 2021, **9**, 65, DOI: **10.3390/vaccines9010065**.

26 K. Liang, R. Ricco, C. M. Doherty, M. J. Styles, S. Bell, N. Kirby, S. Mudie, D. Haylock, A. J. Hill, C. J. Doonan and P. Falcaro, *Nat. Commun.*, 2015, **6**, 7240, DOI: **10.1038/ncomms8240**.

27 N. K. Maddigan, A. Tarzia, D. M. Huang, C. J. Sumby, S. G. Bell, P. Falcaro and C. J. Doonan, *Chem. Sci.*, 2018, **9**, 4217–4223, DOI: **10.1039/c8sc00825f**.
28 R. Singh, M. Musameh, Y. Gao, B. Ozcelik, X. Mulet and C. M. Doherty, *J. Mater. Chem. C*, 2021, **9**, 7677–7688, DOI: **10.1039/d1tc00407g**.
29 M. Eddaoudi, D. F. Sava, J. F. Eubank, K. Adil and V. Guillerm, *Chem. Soc. Rev.*, 2015, **44**, 228–249, DOI: **10.1039/c4cs00230j**.
30 F. Carraro, M. J. Velásquez-Hernández, E. Astria, W. Liang, L. Twight, C. Parise, M. Ge, Z. Huang, R. Ricco, X. Zou and L. Villanova, *Chem. Sci.*, 2020, **11**, 3397–3404, DOI: **10.1039/c9sc05433b**.
31 A. F. Ogata, A. M. Rakowski, B. P. Carpenter, D. A. Fishman, J. G. Merham, P. J. Hurst and J. P. Patterson, *J. Am. Chem. Soc.*, 2020, **2142**, 1433–1442, DOI: **10.1021/jacs.9b11371**.
32 R. Qian, A. Ullah, J. Cui, X. Cai, J. Cao, L. Wu and S. Shen, *Colloids Surf., B*, 2024, **240**, 113980, DOI: **10.1016/j.colsurfb.2024.113980**.
33 Y. H. Wijesundara, T. S. Howlett, S. Kumari and J. J. Gassensmith, *Chem. Rev.*, 2024, **124**, 3013–3036, DOI: **10.1021/acs.chemrev.3c00409**.
34 S. Kumari, T. S. Howlett, R. N. Ehrman, S. Koirala, O. Trashi, I. Trashi, Y. H. Wijesundara and J. J. Gassensmith, *Chem. Sci.*, 2023, **14**, 5774–5782, DOI: **10.1039/d3sc00500c**.
35 L. Wang, G. Zhang, Y. Sun, Z. Wu, C. Ren, Z. Zhang, X. Peng, Y. Zhang, Y. Zhao, C. Li and L. Gao, *ACS Appl. Mater. Interfaces*, 2022, **14**, 46176–46187, DOI: **10.1021/acsami.2c11203**.
36 R. Riccò, W. Liang, S. Li, J. J. Gassensmith, F. Caruso, C. Doonan and P. Falcaro, *ACS Nano*, 2018, **12**, 13–23, DOI: **10.1021/acsnano.7b08056**.
37 R. N. Ehrman, O. R. Brohlin, Y. H. Wijesundara, S. Kumari, O. Trashi, T. S. Howlett, I. Trashi, F. C. Herbert, A. Raja, S. Koirala and N. Tran, *Chem. Sci.*, 2024, **15**, 2731–2744, DOI: **10.1039/d3sc06734c**.
38 S. Bhagchandani, J. A. Johnson and D. J. Irvine, *Adv. Drug Delivery Rev.*, 2021, **175**, 113803, DOI: **10.1016/j.addr.2021.05.013**.
39 F. Ma, J. Zhang, J. Zhang and C. Zhang, *Cell. Mol. Immunol.*, 2010, **7**, 381–388, DOI: **10.1038/cmi.2010.30**.
40 B. Chen, P. Yu, W. N. Chan, F. Xie, Y. Zhang, L. Liang, K. T. Leung, K. W. Lo, J. Yu, G. M. Tse and W. Kang, *Signal Transduction Targeted Ther.*, 2024, **9**, 6, DOI: **10.1038/s41392-023-01679-y**.
41 Y. M. Zhang, J. Zhang, Y. H. Liu, Y. Guo, X. Q. Yu and Z. Huang, *RSC Adv.*, 2020, **10**, 39842–39853, DOI: **10.1039/D0RA08027F**.
42 H. Fang, L. Lin, J. Chen, J. Wu, H. Tian and X. Chen, *Biomater. Sci.*, 2019, **7**, 1716–1728, DOI: **10.1039/C9BM00039A**.
43 X. Nie, W. You, Z. Zhang, F. Gao, X. H. Zhou, H. L. Wang, L. H. Wang, G. Chen, C. H. Wang, C. Y. Hong and Q. Shao, *Adv. Healthcare Mater.*, 2023, **12**, 2203252, DOI: **10.1002/adhm.202203252**.
44 C. Chu, E. Ren, Y. Zhang, J. Yu, H. Lin, X. Pang, Y. Zhang, H. Liu, Z. Qin, Y. Cheng, X. Wang, W. Li, X. Kong, X. Chen and G. Liu, *Angew. Chem.*, 2019, **131**, 275–278, DOI: **10.1002/anie.201812482**.
45 R. M. Zhao, Y. Guo, H. Z. Yang, J. Zhang and X. Q. Yu, *New J. Chem.*, 2021, **45**, 13549–13557, DOI: **10.1039/D1NJ02115J**.
46 S. Chatterjee, E. Kon, P. Sharma and D. Peer, *Proc. Natl. Acad. Sci. U. S. A.*, 2024, **121**, e2307800120, DOI: **10.1073/pnas.2307800120**.
47 Z. Zou, L. He, X. Deng, H. Wang, Z. Huang, Q. Xue, Z. Qing, Y. Lei, R. Yang and J. Liu, *Angew. Chem.*, 2021, **133**, 23152–23158, DOI: **10.1002/anie.202110404**.
48 R. K. DeLong, J. Nava-Chavez, R. Kumar, E. N. Mathew, W. Mwangi and S. Yoon, *ACS Pharmacol. Transl. Sci.*, 2024, **7**, 707–715, DOI: **10.1021/acsptsci.3c00280**.
49 U. Sahin, E. Derhovanessian, M. Miller, B. P. Kloke, P. Simon, M. Löwer, V. Bukur, A. D. Tadmor, U. Luxemburger, B. Schrörs and T. Omokoko, *Nature*, 2017, **547**, 222–226, DOI: **10.1038/nature23003**.
50 X. Wang, S. Liu, Y. Sun, X. Yu, S. M. Lee, Q. Cheng, T. Wei, J. Gong, J. Robinson, D. Zhang and X. Lian, *Nat. Protoc.*, 2023, **18**, 265–291, DOI: **10.1038/s41596-022-00755-x**.
51 L. Schoenmaker, D. Witzigmann, J. A. Kulkarni, R. Verbeke, G. Kersten, W. Jiskoot and D. J. A. Crommelin, *Int. J. Pharm.*, 2021, **601**, 120586, DOI: **10.1016/j.ijpharm.2021.120586**.